

Testing Properties of the Galactic Center Black Hole Using Stellar Orbits

David Merritt*

*Department of Physics and Center for Computational Relativity and Gravitation,
Rochester Institute of Technology, Rochester, NY 14623*

Tal Alexander†

Faculty of Physics, Weizmann Institute of Science, POB 26, Rehovot, Israel

Seppo Mikkola‡

Tuorla Observatory, University of Turku, Väisäläntie 20, Piikkiö, Finland

Clifford M. Will§

McDonnell Center for the Space Sciences, Department of Physics, Washington University, St. Louis, MO 63130

(Dated: October 24, 2018)

The spin and quadrupole moment of the supermassive black hole at the Galactic center can in principle be measured via astrometric monitoring of stars orbiting at milliparsec (mpc) distances, allowing tests of general relativistic “no-hair” theorems [1]. One complicating factor is the presence of perturbations from other stars, which may induce orbital precession of the same order of magnitude as that due to general relativistic effects. The expected number of stars in this region is small enough that full N -body simulations can be carried out. We present the results of a comprehensive set of such simulations, which include a post-Newtonian treatment of spin-orbit effects. A number of possible models for the distribution of stars and stellar remnants are considered. We find that stellar perturbations are likely to obscure the signal due to frame-dragging for stars beyond ~ 0.5 mpc from the black hole, while measurement of the quadrupole moment is likely to require observation of stars inside ~ 0.2 mpc. A high fraction of stellar remnants, e.g. $10M_{\odot}$ black holes, in this region would make tests of GR problematic at all radii. We discuss the possibility of separating the effects of stellar perturbations from those due to GR.

PACS numbers: Valid PACS appear here

I. INTRODUCTION

The supermassive black hole (SBH) at the center of the Milky Way galaxy is surrounded by a compact cluster of stars that has been the target of observational surveys for more than a decade [2, 3, 4, 5, 6, 7]. Near-infrared monitoring of stellar positions using adaptive optics techniques has allowed orbital reconstruction for roughly 30 stars at distances ranging from $10^0 - 10^2$ milliparsecs (mpc) from the SBH [8, 9, 10]. One of these stars (S2) has an orbital period of only ~ 15 yr [11, 12] and its orbit has been followed for more than one full revolution; astrometric data for S2 yield a well-constrained mass for the SBH, $M_{\bullet} = (3.95 \pm 0.06) \times 10^6 M_{\odot}$ (assuming a galactocentric distance of 8.0 kpc) and a location on the plane of the sky that is consistent with that of the radio source Sgr A* [9, 10, 13, 14, 15, 16].

The velocity of S2 near periastron is a few percent of the speed of light, large enough that relativistic effects like advance of the periastron become potentially measurable, even on time scales as short as a few years [17, 18, 19, 20].

No such effects have so far been unambiguously observed [16]; one complicating factor is the likely presence of a distributed mass (stars, stellar remnants, dark matter etc.) within S2’s orbit which could produce Newtonian precession of the same order of magnitude as that due to general relativity [21, 22].

If the SBH is rotating, new phenomena occur for stars orbiting at very small separations, $r \lesssim 1$ mpc. Dragging of inertial frames and torques from the SBH’s quadrupole moment Q cause stellar orbital planes to precess, at rates that depend respectively on the first and second powers of the hole’s spin angular momentum \mathbf{J} . These spin-related effects are small compared with in-plane precession, but (in the absence of other non-spherically-symmetric components of the gravitational potential) they contain unambiguous information about \mathbf{J} and Q . In principle, observed changes in the orbital orientations of just two stars would be sufficient to independently constrain the four quantities (\mathbf{J} , Q), allowing tests of general relativistic “no-hair” theorems [1]. The amplitude of these spin-related precessions is very small, of order microarcseconds (μas) per year as seen from the Earth. Plans are being developed to achieve infrared astrometry at this level [23, 24].

Such measurements will require the presence of at least a few bright stars on mpc-scale orbits around the SBH. While no such stars have yet been observed, extrapo-

*Electronic address: merritt@astro.rit.edu

†Electronic address: tal.alexander@weizmann.ac.il

‡Electronic address: mikkola@utu.fi

§Electronic address: cmw@wuphys.wustl.edu

lation of the observed stellar densities at distances of ~ 1 pc from the SBH suggests that of order $10^0 - 10^2$ stars should be present in this region. Due to their finite numbers, these stars will generate a non-spherically-symmetric component to the gravitational potential with an amplitude that scales as $\sqrt{Nm_\star}$, where m_\star is the mass of a typical star and N is their number. Simple arguments (§II) suggest that such stellar perturbations might produce changes in the orbital orientations of test stars that are comparable in magnitude to the spin-related effects. This would complicate the testing of no-hair theorems by adding what is effectively a source of noise to the measured precessions.

Because the expected number of stars in this region is so small, direct N -body integration of the equations of motion for all N stars is feasible. The major technical requirements are a high degree of accuracy in the N -body integrator and the inclusion of terms describing the relativistic accelerations due to the SBH, including spinless, spin-orbit, and quadrupole-orbit contributions.

Here we present the results of a comprehensive set of such simulations. Our primary goal is to evaluate the degree to which star-star perturbations might obscure the signal due to the SBH's spin; hence we focus on changes in orbital orientations rather than on the evolution of the phase-space variables (\mathbf{r}, \mathbf{v}) [25, 26]. We ignore all other systematic effects that might limit the ability to carry out the high-precision astrometry for stars in crowded fields at the Galactic center [19, 27].

In §II we summarize the relevant time scales for orbital evolution near the Milky Way SBH. §III presents the post-Newtonian N -body equations of motion including the lowest-order spin-orbit terms and describes the N -body integrator. Observational and theoretical constraints on the distribution of stars and stellar remnants near the Galactic center SBH are summarized in §IV, which also describes the parametrized models used to construct the N -body initial conditions. §V summarizes the results from the integrations, including estimates of the number of stars that can be effectively used to measure \mathbf{J} and Q . §VI discusses how the presence of stellar perturbations in the astrometric data can potentially be detected and removed from the GR signal. §VII sums up.

II. SOURCES OF ORBITAL EVOLUTION

A. Basic quantities

The orbital period of a star of semi-major axis a orbiting around the Milky Way SBH is

$$P = \frac{2\pi a^{3/2}}{\sqrt{GM_\bullet}} \approx 1.48 \tilde{a}^{3/2} \text{yr} \quad (1)$$

where M_\bullet is the mass of the SBH and \tilde{a} is the star's semi-major axis in units of milli-parsecs (mpc). The second

relation assumes $M_\bullet = 4.0 \times 10^6 M_\odot$ and $m_\star \ll M_\bullet$, assumptions which we adopt in the remainder of the paper. The length scale associated with the event horizon of the SBH is

$$r_g \equiv \frac{GM_\bullet}{c^2} \approx 1.92 \times 10^{-4} \text{mpc}. \quad (2)$$

We define χ to be the dimensionless spin angular momentum vector of the SBH,

$$\mathbf{J} = \chi \left(\frac{GM_\bullet^2}{c} \right), \quad 0 \leq \chi \leq 1. \quad (3)$$

The standard (no-hair) relation between J and the quadrupole moment is

$$Q = -\frac{1}{c} \frac{J^2}{M_\bullet}. \quad (4)$$

We adopt this relation below unless otherwise noted.

In the regime of interest, stellar orbits around the SBH can be approximated as Keplerian ellipses that experience gradual changes in their orbital elements, due both to the effects of relativity and to perturbations from other stars. Here we summarize the relevant sources of evolution and their associated time scales under this approximation.

B. Relativistic precession

1. In-plane precession

In the orbit-averaged approximation, massless test particles orbiting a black hole experience advance of the orbital periapse by an angle [80]

$$\delta\varpi = A_S - 2A_J \cos i - \frac{1}{2} A_Q (1 - 3 \cos^2 i) \quad (5)$$

per orbit, where the subscripts S, J, Q denote the effects due to the black holes's mass (i.e. the Schwarzschild part of the metric), spin and quadrupole moment (the Kerr part of the metric) respectively and i is the orbital inclination, defined as the angle between the SBH spin vector and the stellar orbital angular momentum vector. To lowest post-Newtonian PN order,

$$A_S = \frac{6\pi}{c^2} \frac{GM_\bullet}{(1-e^2)a} \approx 12.4' (1-e^2)^{-1} \tilde{a}^{-1}, \quad (6a)$$

$$A_J = \frac{4\pi\chi}{c^3} \left[\frac{GM_\bullet}{(1-e^2)a} \right]^{3/2} \approx 0.115' (1-e^2)^{-3/2} \chi \tilde{a}^{-3/2}, \quad (6b)$$

$$A_Q = \frac{3\pi\chi^2}{c^4} \left[\frac{GM_\bullet}{(1-e^2)a} \right]^2 \approx 1.19' \times 10^{-3} (1-e^2)^{-2} \chi^2 \tilde{a}^{-2} \quad (6c)$$

where e is the orbital eccentricity. Since the Schwarzschild contribution exceeds in amplitude the spin- and quadrupole contributions to the in-plane precession for $a(1 - e^2) \gtrsim 10^{-4}$ mpc $\approx r_g$, advance of the periastron does not contain much useful information about the SBH spin [1].

We define the precession time scale due to the Schwarzschild term alone as

$$t_S \equiv \left[\frac{A_S(a, e)}{\pi P(a)} \right]^{-1} \quad (7a)$$

$$= \frac{P}{6} \frac{c^2 a}{GM_\bullet} (1 - e^2) \quad (7b)$$

$$\approx 1.29 \times 10^3 \text{yr} (1 - e^2) \tilde{a}^{5/2}. \quad (7c)$$

The Schwarzschild contribution to the in-plane precession is large enough to potentially be detectable via a few years' monitoring of identified stars at ~ 10 mpc separations from the SBH [18, 20, 21].

2. Precession of orbital planes

The gravitational field of a Kerr black hole is not spherically symmetric. The dominant non-spherically-symmetric effect on test-particle orbits is the coupling between the spin of the black hole and the orbital angular momentum of the particle, known in the weak-field limit as the Lense-Thirring effect [28, 29]. Again to lowest PN order, the change per orbit of the nodal angle Ω is [1]

$$\delta\Omega = A_J - A_Q \cos i \quad (8)$$

[81]. Among relativistic effects, precession of orbital planes depends only on \mathbf{J} and Q . We note that the frame dragging contribution in Eq. (8), which dominates at most distances of interest here, is independent of orbital inclination while the quadrupole-induced precession is inclination-dependent. Both precessions leave the inclination with respect to the black hole spin unchanged.

Defining the associated time scales as in Eq. (7), we find

$$t_J = \frac{P}{4\chi} \left[\frac{c^2 a (1 - e^2)}{GM_\bullet} \right]^{3/2} \quad (9a)$$

$$\approx 1.39 \times 10^5 \text{yr} (1 - e^2)^{3/2} \chi^{-1} \tilde{a}^3, \quad (9b)$$

$$t_Q = \frac{P}{3\chi^2} \left[\frac{c^2 a (1 - e^2)}{GM_\bullet} \right]^2 \quad (9c)$$

$$\approx 1.34 \times 10^7 \text{yr} (1 - e^2)^2 \chi^{-2} \tilde{a}^{7/2}. \quad (9d)$$

Figure 1 plots t_J and t_Q as functions of a and e .

C. Stellar perturbations

If there is a star cluster around the SBH, the smooth contribution to the gravitational force from the dis-

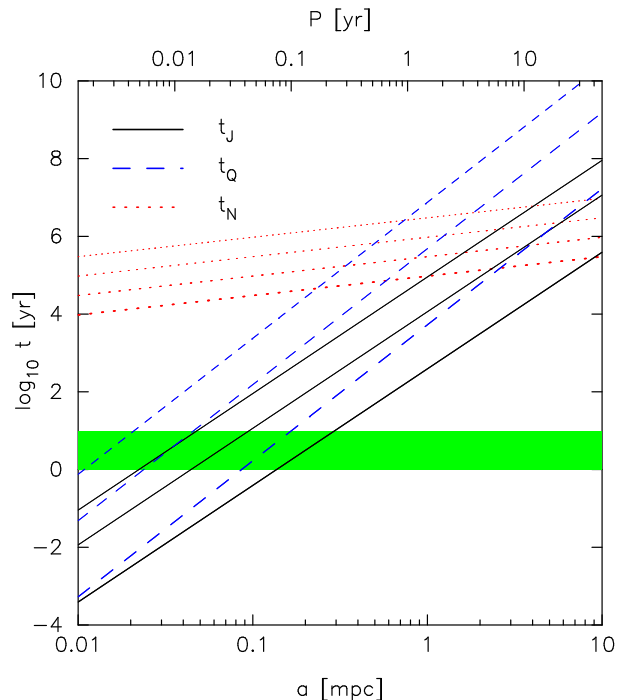


FIG. 1: Time scales associated with precession of orbital planes about the Galactic supermassive black hole. t_J, t_Q : precession time scales due to frame-dragging and to the quadrupole torque from a maximally-spinning SBH. Line thickness denotes orbital eccentricity, from $e = 0.99$ (thickest) to $e = 0.5$ (thinnest). t_N : approximate precessional time scale due to Newtonian perturbations from other stars, assumed to have one Solar mass. Line thickness denotes total distributed mass within 1 mpc from the SBH, from $10^3 M_\odot$ (thickest) to $1 M_\odot$ (thinnest), assuming that density falls off as r^{-1} . Shaded (green) region shows range of interesting time intervals for observation, $1 \text{ yr} \leq \Delta t \leq 10 \text{ yr}$.

tributed mass breaks the degeneracy between radial and angular periods in the classical Kepler problem, causing an in-plane precession, in the opposite sense to the relativistic periastron advance. Assuming that the stellar mass density follows $r^{-\gamma}$, with r the distance from the SBH, the advance of orbital periastron in one period is

$$\delta\varpi \approx 2\pi \frac{M_\star(a)}{M_\bullet} \sqrt{1 - e^2} F(\gamma) \quad (10)$$

where $M_\star(r)$ is the distributed mass enclosed within radius r and $F = (3/2, 1)$ for $\gamma = (0, 1)$ [30]. Setting $F \approx 1$, the associated time scale is

$$t_M \approx \frac{P M_\bullet}{2 M_\star} (1 - e^2)^{-1/2} \quad (11a)$$

$$\approx 3.0 \times 10^6 \text{yr} \tilde{M}_\star^{-1} \tilde{a}^{\gamma-3/2} (1 - e^2)^{-1/2} \quad (11b)$$

where \tilde{M}_\star is the stellar mass within 1 mpc in units of the solar mass. This time scale is long compared with the time t_S for relativistic periastron advance, Eq. (7), at all radii of interest unless M_\star is unphysically large.

The discrete nature of the stellar cluster adds an additional, non-spherically-symmetric component to the gravitational potential, which can induce precession in orbital planes that mimics the effects of frame-dragging and quadrupole torques. In the case that the time scale associated with this precession is long compared with both the radial period (Eq. 1) and with the time scale for in-plane periastron advance (Eq. 7) (assumptions that will be verified below), orbits around the SBH respond to the finite- N component of the gravitational force as if they were annuli, changing their orientations but not their eccentricities (“vector resonant relaxation”; [31]).

Here we estimate the rate of precession due to finite- N stellar perturbations, adopting a purely Newtonian model for star-star interactions.

Let $q \equiv m_*/M_\bullet$ be the ratio between stellar mass and SBH mass, N the number of stars and/or stellar remnants in the region contained within a test star’s orbit (a more precise definition of N is adopted in §IV) and L_c the angular momentum of a circular orbit of the same energy as that of the test star. In the vector resonant relaxation (RR) regime, orbital angular momenta evolve approximately as [31]

$$\frac{|\Delta\mathbf{L}|}{L_c} \approx \beta_v q \sqrt{N} \frac{\Delta t}{P} \quad (12)$$

for a time $\Delta t \lesssim t_{\text{coh}}$, where β_v is a constant of order unity and t_{coh} is the time scale associated with the most rapid process that randomizes orbital planes, thus breaking the coherence.

In the absence of GR effects, the only source of coherence-breaking is the stellar perturbations themselves (“self-quenching”), for which $t_{\text{coh}} = t_N$, where t_N is defined by the condition $|\Delta\mathbf{L}|/L_c(t_N) = 1$. On time scales long compared to t_N , and in the absence of frame-dragging or other torques, orbital orientations would evolve approximately as

$$\frac{|\Delta\mathbf{L}|}{L_c} \approx \beta_v q \sqrt{N} \frac{\sqrt{t_{\text{coh}} \Delta t}}{P}, \quad (13)$$

i.e. as $(\Delta t)^{1/2}$ rather than as $(\Delta t)^1$. Fig. 1 shows that t_N is $\gtrsim 10^4$ yr for reasonable models of the stellar cluster, much longer than the ~ 10 yr time scales of interest here; hence the self-quenched regime is irrelevant in what follows.

However at some radius, t_N will exceed the time scales associated with GR precession of orbital planes, and the precession rate will be given by the expressions derived in the previous section rather than by Eq. (12). To estimate this radius, we begin by expressing the GR precessional time scales defined above in terms of the “penetration parameter” $\varrho \equiv (1+e)r_p/r_g > 1$, where r_p is the Keplerian orbital periastron distance and r_g is defined in Eq. (2). The results are:

$$t_J = \frac{1}{4} \varrho^{3/2} \chi^{-1} P, \quad (14a)$$

$$t_Q = \frac{1}{3} \varrho^2 \chi^{-2} P \quad (14b)$$

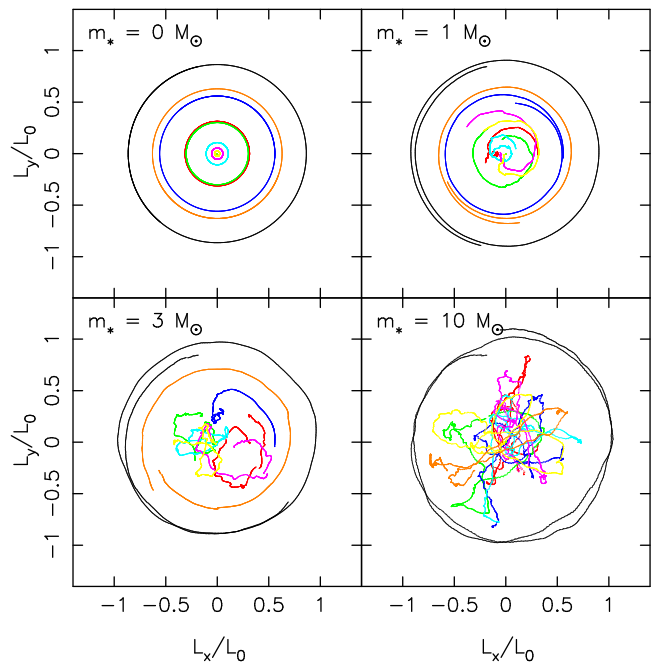


FIG. 2: Evolution of orbital planes in a cluster of eight stars orbiting about the Galactic center SBH, for an elapsed time of 2×10^6 years. The SBH rotates about the z -axis with maximal spin. Four different values were assumed for the stellar masses m_* , as indicated. Stars were placed initially on orbits with semi-major axis 2 mpc and eccentricity 0.5 and with random orientations.

and the vector RR time scale itself is

$$t_N \approx \frac{1}{q\sqrt{N}} P; \quad (14c)$$

the latter expression is true only up to $\mathcal{O}(1)$ factors which have to be derived from simulations.

Since

$$\frac{t_Q}{t_J} = (4/3\chi)\varrho^{1/2} \geq 4/3, \quad (15)$$

precession due to frame-dragging is everywhere faster than precession due to the quadrupole torque.

The condition that frame dragging dominate stellar perturbations is approximately

$$\frac{t_N}{t_J} \approx \frac{4\chi}{q\sqrt{N}\varrho^{3/2}} > 1. \quad (16)$$

Fig. 1 shows that for $\chi = 1$, this condition is satisfied inside ~ 1 mpc for reasonable values of the enclosed mass. For $\chi < 1$, the critical radius is smaller. This justifies looking at stellar perturbations as a source of “noise” in tests of GR.

D. Comparing relativistic and Newtonian precessions

Precession of orbital planes induced by stellar perturbations differs qualitatively from precession due to frame dragging since it does not respect the direction of the SBH spin axis. Fig. 2 shows the results of a set of 2×10^6 yr integrations (using the algorithm described in §III) that illustrate the difference. When the stellar masses are set to zero, orbital angular momenta exhibit the uniform precession about the SBH's spin axis associated with frame dragging; when stellar masses are increased, the orbital angular momentum vectors move quasi-randomly about the unit sphere.

In comparing GR precession with that due to stellar perturbations, it is therefore useful to have a measure of orientation that is invariant to the direction of the SBH spin. We adopt $\Delta\theta$, defined as the angle between the initial and final orbital angular momentum vectors:

$$\cos \Delta\theta = \frac{\mathbf{L}_i \cdot \mathbf{L}_f}{L_i L_f}. \quad (17)$$

On time scales of relevance here, $|\mathbf{L}|$ is conserved, i.e. $L_i \approx L_f$, because the time scales for both non-resonant and resonant relaxation are much longer than 10 yr.

Precession induced by GR changes only the nodal angle Ω (Eq. 8). Since

$$\mathbf{L} = L (\sin \Omega \sin i \mathbf{e}_x + \cos \Omega \sin i \mathbf{e}_y + \cos i \mathbf{e}_z), \quad (18)$$

where the z -axis is parallel to the SBH spin vector, $L_i = L_f$ implies

$$\cos \Delta\theta_{GR} = \cos^2 i + \sin^2 i \cos \Delta\Omega \quad (19)$$

which for small $\Delta\Omega$ is

$$\Delta\theta_{GR} \approx \sin i \Delta\Omega. \quad (20)$$

In the case of star-star perturbations, we need to express $\Delta\theta$ in terms of $\Delta\mathbf{L}/L_c$. By definition,

$$|\Delta\mathbf{L}|^2 = L_i^2 + L_f^2 - 2L_i L_f \cos \Delta\theta \quad (21)$$

so

$$\frac{|\Delta\mathbf{L}|^2}{L_c^2} = 2 \frac{L^2}{L_c^2} (1 - \cos \Delta\theta) \quad (22a)$$

$$\approx \frac{L^2}{L_c^2} (\Delta\theta)^2 \quad (22b)$$

where the last expression again assumes small $\Delta\theta$.

Specializing Eq. (20) to the case of frame dragging, we note that $\Delta\Omega$ is independent of $\cos i$. Considering orbits with a single eccentricity e and with an isotropic distribution of inclinations, the rms values of the angles in Eq. (20) are therefore related by

$$\Delta\theta_J \approx \sqrt{\frac{2}{3}} \Delta\Omega \quad (23)$$

or (cf. Eq. 6b)

$$\Delta\theta_J \approx 4\pi \sqrt{\frac{2}{3}} \chi \varrho^{-3/2} \frac{\Delta t}{P}. \quad (24)$$

In the case of quadrupole-induced precession, $\Delta\Omega \propto \cos i$. Again computing the rms values assuming random orientations gives

$$\Delta\theta_Q \approx \sqrt{\frac{6}{5}} \pi \chi^2 \varrho^{-2} \frac{\Delta t}{P}. \quad (25)$$

Finally, for stellar perturbations, we ignore a possible dependence of $|\Delta\theta_N|$ on orbital eccentricity. In an isotropic cluster, the orbital angular momenta at any energy (\sim radius) are distributed as $n(L)dL = 2LdL/L_c^2$, so $\langle L^2 \rangle / L_c^2 = 1/2$, and the rms values in Eq. (22) are related by

$$\Delta\theta_N \approx \sqrt{2} \frac{|\Delta\mathbf{L}|}{L_c}. \quad (26)$$

Using Eq. (12), this can be written

$$\Delta\theta_N \approx \sqrt{2} \beta_v q \sqrt{N} \frac{\Delta t}{P}. \quad (27)$$

Eilon et al. [32] give $\beta_v \approx 1.8$ as an average value for a cluster with isotropically distributed velocities, if N is defined as the number of stars within a sphere of radius $r = a$. We can then write a slightly more accurate definition of the vector RR time scale (again defined as the time such that $\Delta\theta_N = \pi$),

$$t_N = \frac{\pi}{\sqrt{2} \beta_v q \sqrt{N}} P \approx \frac{1.2}{q \sqrt{N}} P. \quad (28)$$

This is the expression plotted in Fig. 1.

We have assumed that precession is due either to GR spin effects or to stellar perturbations. In reality, one expects vector RR to be quenched somewhat by coherence-breaking due to GR precession even at radii where $t_N < t_{J,Q}$.

Equating (24) with (27), we obtain an approximate expression for the radius at which frame-dragging dominates stellar perturbations:

$$\varrho^{3/2} \sqrt{N} \approx \frac{4\pi}{\sqrt{3} \beta_v} \frac{\chi}{q} \quad (29)$$

i.e.

$$r_{\text{crit}} \approx 1 \text{mpc} (1 - e^2)^{-1} \chi^{2/3} \left(\frac{N_{\text{crit}}}{30} \right)^{-1/3} \left(\frac{m_\star}{10 M_\odot} \right)^{-2/3} \quad (30)$$

where N_{crit} is the number of stellar perturbers within r_{crit} of mass m_\star each. We evaluate this expression in §IV after specifying a model for the stellar distribution, and in §V we present the results of full N -body simulations that allow more precise estimates of r_{crit} .

III. *N*-BODY TREATMENT

Integrations of the *N*-body equations of motion were carried out using algorithmic regularization [33, 34] implemented with a chain structure [35] and the time-transformed leapfrog [36]. The algorithm produces exact trajectories for Newtonian two-body motion and regular results for close encounters involving arbitrary numbers of bodies. Velocity-dependent forces were included via a generalized mid-point method [37]; the ARCHAIN code [38] also incorporates pairwise post-Newtonian forces for non-

spinning particles of orders up to and including PN2.5 [39]. We included PN terms in the interactions between the SBH particle and the *N* − 1 “star” particles. All *N* particles were included at all times in the chain. Accumulated energy errors were never more than a few parts in 10¹⁰.

We modified ARCHAIN to include the lowest-order contributions of the SBH’s spin and quadrupole moment to the motions of the stars. In the covariant spin supplementary condition (SSC) gauge [40], the spin-related, *N*-body accelerations \mathbf{a}_J are

$$\mathbf{a}_{J,1} = -\frac{3G^2 M_\bullet}{c^3} \sum_{j \neq 1} \frac{m_j}{r_{1j}^3} \left\{ [\mathbf{v}_{1j} - (\mathbf{n}_{1j} \cdot \mathbf{v}_{1j}) \mathbf{n}_{1j}] \times \boldsymbol{\chi} - 2\mathbf{n}_{1j} (\mathbf{n}_{1j} \times \mathbf{v}_{1j}) \cdot \boldsymbol{\chi} \right\}, \quad (31a)$$

$$\mathbf{a}_{J,j} = \frac{2G^2 M_\bullet^2}{c^3 r_{1j}^3} \left\{ [2\mathbf{v}_{1j} - 3(\mathbf{n}_{1j} \cdot \mathbf{v}_{1j}) \mathbf{n}_{1j}] \times \boldsymbol{\chi} - 3\mathbf{n}_{1j} (\mathbf{n}_{1j} \times \mathbf{v}_{1j}) \cdot \boldsymbol{\chi} \right\}, \quad (31b)$$

$$\dot{\boldsymbol{\chi}} = \frac{G}{2c^2} \sum_{j \neq i} \frac{m_j}{r_{ij}^2} [\mathbf{n}_{1j} \times (3\mathbf{v}_1 - 4\mathbf{v}_j)] \times \boldsymbol{\chi}, \quad (31c)$$

$$r_{ij} \equiv |\mathbf{x}_i - \mathbf{x}_j|, \quad \mathbf{x}_{ij} \equiv \mathbf{x}_i - \mathbf{x}_j, \quad \mathbf{n}_{ij} = \mathbf{x}_{ij}/r_{ij}, \quad \mathbf{v}_{ij} \equiv \mathbf{v}_i - \mathbf{v}_j. \quad (31d)$$

Here, particle number 1 is the SBH and particles *j*, 2 ≤ *j* ≤ *N* are the stars. The “linear momentum” that is conserved by these equations is

$$\mathbf{P} = \sum_i m_i \mathbf{v}_i + \frac{G}{c^2} \sum_{ij} \frac{m_i}{2r_{ij}^3} (\mathbf{x}_{ij} \times \mathbf{J}_j). \quad (32)$$

Adopting Eq. (4) for the SBH quadrupole moment, the equation of motion for the *j*th particle has the additional term $\mathbf{a}_{Q,j}$, where

$$\mathbf{a}_{Q,j} = +\frac{3}{2} \chi^2 \frac{G^3 M_\bullet^3}{c^4 r^4} \left[5\mathbf{n}_{1j} (\mathbf{n}_{1j} \cdot \hat{\mathbf{J}})^2 - 2(\mathbf{n}_{1j} \cdot \hat{\mathbf{J}}) \hat{\mathbf{J}} - \mathbf{n}_{1j} \right], \quad \hat{\mathbf{J}} \equiv \mathbf{J}/J. \quad (33)$$

IV. MODELS FOR THE STELLAR DISTRIBUTION

A. Observational constraints

The distribution of stars and stellar remnants at distances ≪ 1 pc from the Galactic center SBH is poorly understood. Only the brightest stars in the inner parsec have been identified, via speckle or adaptive optics imaging and spectroscopy in the near-infrared bands [41, 42]. Most of these stars appear to belong to one of two distinct populations: (1) “early-type” (ET) stars – apparently normal, upper-main-sequence giant stars of O and B spectral types with inferred masses of 7–80*M*_⊙ and ages less than the main-sequence turnoff age, i.e. *O*[10¹–10²] Myr; and (2) “late-type” (LT) stars – old, metal-rich, M, K and G-spectral-type giant (post-main-sequence) stars

with ages *O*[10⁰–10¹] Gyr and masses 1–2*M*_⊙. The density of ET stars increases steeply toward the SBH and these stars account for a large part of the total luminosity of the central cluster, but their total numbers are small, roughly 10² in the inner 0.1 pc [6, 10, 43] with few if any on orbits that bring them within ∼ 10 mpc from the SBH, making them unlikely candidates either as test stars for observing GR spin effects or as perturbers of the test stars.

The LT stars on the other hand are believed to be characteristic of the dominant, old population; roughly 6000 LT stars have been identified in the inner ∼ 0.5 pc and their K-band luminosity function suggests a roughly continuous star formation history over the last ∼ 10 Gyr [43, 44]. In spite of their large numbers, the observed LT stars appear to be weakly concentrated toward the SBH. Number counts complete to *K* ≈ 15.5 (corresponding

to the sub-giant phase for $1\mathcal{M}_\odot$ stars) reveal a projected density that is flat or declining inside a projected distance of ~ 0.5 pc from the SBH [43, 45, 46]. While the existence of four LT stars on very tight ($5 \text{ mpc} \lesssim a \lesssim 20 \text{ mpc}$) orbits around the SBH has been established [10], deprojection of the binned surface density profile implies a central space density that is consistent with zero at distances smaller than ~ 0.1 pc from the SBH [47].

The low density of LT stars in the inner parsec is not well understood. If the time scale for exchange of orbital kinetic energy between stars (the two-body relaxation time; [48]) is shorter than several Gyr, one expects the stellar distribution to have attained a quasi-steady-state distribution of the form $n(r) \sim r^{-\gamma}$, $3/2 \lesssim \gamma \lesssim 7/4$ [49, 50] within the SBH gravitational influence radius, $r_{\text{infl}} \equiv GM_\bullet/\sigma_\star^2 \approx 10^0$ pc. This is clearly not observed [45], suggesting either that the relaxation time exceeds ~ 10 Gyr throughout the inner parsec, or that the brightest stars have been hidden from view or destroyed. Collisions with main-sequence stars or stellar remnants can remove the outer envelopes of red-giant stars, potentially explaining the low observed density of giants [42]. However this mechanism only appears to be effective at distances less than ~ 0.1 pc from the SBH [51, 52, 53], even assuming a high density for the colliding populations (an assumption for which there is currently no observational support). Even at these radii, collisions would seem to be ineffective at explaining the depletion of stars down to magnitudes as faint as 15.5 [53].

It has been argued that the stellar initial mass function (IMF) may have been strongly truncated below $\sim 3\mathcal{M}_\odot$ in the Galactic center region [54, 55]. These are just the stars that would dominate the K-band number counts now [53].

At the high-mass end, standard IMFs [56, 57] predict that $\sim 0.1\%$ of stars have initial masses greater than $20\mathcal{M}_\odot$, ending their short lives as $\sim 5 - 15\mathcal{M}_\odot$ black holes (BHs). The BHs are expected to segregate nearer to the SBH than the lower-mass components (stars, white dwarves, neutron stars [58]), possibly dominating the total number density inside ~ 1 mpc [52, 59, 60] and providing the bulk of the perturbations acting on the observed stars in this region. However if the observed distribution of late-type stars is a guide, the two-body relaxation time may be too long for establishment of a mass-segregated distribution [47, 52, 61]. If this is the case, there is no compelling reason to assume that the ratio of BHs to stars is as large as implied by the mass-segregated models.

Proper motion studies of large samples of LT stars in the inner parsec [62, 63] yield dynamical constraints on the distributed mass (stars, stellar remnants, gas etc.) in this region. The proper motion data robustly require an extended mass of $\sim 0.5 - 1.5 \times 10^6 \mathcal{M}_\odot$ within the central parsec [63]. However these data do not strongly constrain the radial dependence of the distributed mass density nor the amount of mass on the mpc scales of interest here.

TABLE I: Parameters of the N -body models

| γ | β | \tilde{M}_\star | \mathcal{R} | \tilde{a}_{max} | N_{MS} | N_{BH} | N_{rand} |
|----------|---------|-------------------|---------------|--------------------------|-----------------|-----------------|-------------------|
| 0 | -1 | 10 | 0 | 4.0 | 159 | 0 | 6 |
| 0 | -1 | 10 | 0.1 | 4.0 | 79 | 8 | 12 |
| 0 | -1 | 10 | 1 | 4.0 | 14 | 15 | 70 |
| 1 | -1 | 10 | 0 | 4.0 | 119 | 0 | 8 |
| 1 | -1 | 10 | 0.1 | 4.0 | 59 | 6 | 16 |
| 1 | -1 | 10 | 1 | 4.0 | 10 | 11 | 90 |
| 1 | 0 | 30 | 0 | 3.5 | 183 | 0 | 6 |
| 1 | 0 | 30 | 0.1 | 4.0 | 119 | 12 | 8 |
| 1 | 0 | 30 | 1 | 4.0 | 21 | 22 | 45 |
| 2 | -1 | 30 | 0 | 4.0 | 119 | 0 | 8 |
| 2 | -1 | 30 | 0.1 | 4.0 | 59 | 6 | 15 |
| 2 | -1 | 30 | 1 | 4.0 | 10 | 11 | 100 |
| 2 | 0 | 10 | 1 | 4.0 | 4 | 3 | 300 |
| 2 | 0 | 30 | 0 | 4.0 | 119 | 0 | 8 |
| 2 | 0 | 30 | 0.1 | 4.0 | 59 | 6 | 15 |
| 2 | 0 | 30 | 1 | 4.0 | 10 | 11 | 100 |
| 2 | 0 | 100 | 0 | 1.75 | 174 | 0 | 6 |
| 2 | 0 | 100 | 0.1 | 4.0 | 179 | 19 | 6 |
| 2 | 0 | 100 | 1 | 4.0 | 36 | 36 | 30 |
| 2 | 0.5 | 100 | 0 | 1.75 | 174 | 0 | 6 |
| 2 | 0.5 | 100 | 0.1 | 4.0 | 179 | 19 | 6 |
| 2 | 0.5 | 100 | 1 | 4.0 | 36 | 36 | 30 |

B. Parametrized models

Given these uncertainties, we explored a range of different models for the distribution of stars and stellar remnants near the Galactic SBH. We define M_\star as the distributed mass within 1 mpc from the SBH and $\tilde{M}_\star \equiv M_\star/\mathcal{M}_\odot$. We idealize the stellar populations in this region as consisting of just two components: $1\mathcal{M}_\odot$ main-sequence (MS) stars and $10\mathcal{M}_\odot$ BHs. The first population is assumed to be amenable to astrometric monitoring, and all discussions of orbital evolution presented below will refer to this population. While the orbits of the BHs are also allowed to evolve in our models, we do not describe that evolution in what follows.

In addition to M_\star , three additional parameters define the initial distributions of stars and stellar remnants in our models:

- the power-law index γ describing the number density profiles, $n(r) \propto r^{-\gamma}$; γ is assumed to be the same for both MS stars and BHs;
- the (number) ratio \mathcal{R} of BHs to MS stars, i.e. $\mathcal{R} = N_{\text{BH}}/N_{\text{MS}}$;
- the velocity anisotropy β , defined such that $\sigma_r^2/\sigma_t^2 = (1 - \beta)^{-1}$, where σ_r and σ_t are respectively the 1d velocity dispersions in directions parallel and perpendicular to the radius vector; $\beta = 0$ corresponds to isotropy.

For M_\star we adopted one of the three values $(10, 30, 100)\mathcal{M}_\odot$; the latter value is roughly the enclosed

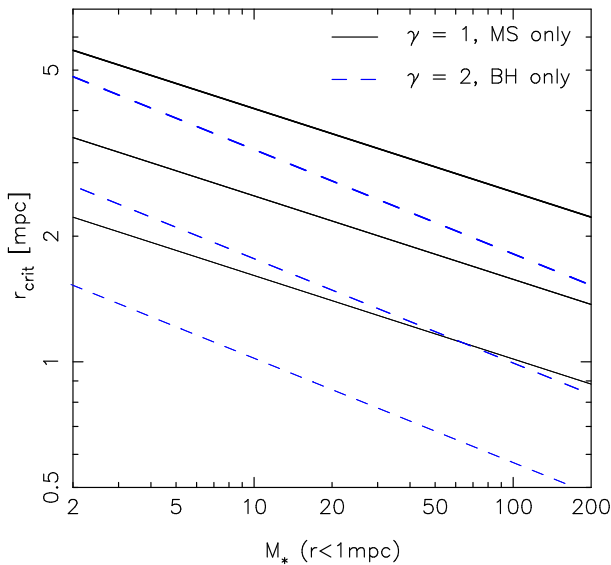


FIG. 3: Approximate value of the radius at which stellar perturbations match frame dragging in terms of their ability to change the direction of orbital angular momenta (Eq. 29). Two models for the stellar cluster are shown: a steeply-rising density profile, $\gamma = 2$, that is dominated by $10M_{\odot}$ stellar black holes; and a shallower density profile, $\gamma = 1$, dominated by $1M_{\odot}$ main-sequence stars. Horizontal axis is the total distributed mass within 1 mpc from the SBH. Line widths denote SBH spin: $\chi = 1$ (thickest), $\chi = 0.3$, and $\chi = 0.1$ (thinnest).

mass predicted by the relaxed, mass-segregated models cited above. For γ we considered the values $(0, 1, 2)$; $\gamma = 0$ corresponds to a constant density in the inner mpc, roughly what is observed in the projected density of LT stars,[82] while $\gamma = 2$ is approximately the value expected for a mass-segregated population around a SBH. Adopting the proper-motion result that the distributed mass within 1 pc is $\sim 10^6 M_{\odot}$ [63], the implied mass inside 1 mpc is $\sim 10^0(10^3)M_{\odot}$ for $\gamma = (1, 2)$. We therefore associated larger values of \tilde{M}_{\star} with larger values of γ , although as noted above, the proper-motion data do not directly constrain the mass distribution on mpc scales. \mathcal{R} was set to $(0, 0.1, 1)$; $\mathcal{R} = 1$ is roughly the largest value predicted in the mass-segregated models assuming a standard IMF, while $\mathcal{R} \approx 10^{-3}$ is expected in the absence of any mass segregation. For the small ($\sim 10^2$) total particle numbers in the N -body simulations, $\mathcal{R} = 0$ is essentially the same as $\mathcal{R} = 10^{-3}$.

A steady-state orbital distribution in a point-mass potential requires $\beta < \gamma - 1/2$, i.e., isotropic velocity distributions are not permitted when $\gamma < 0.5$: the distribution of orbital eccentricities must be biased toward small values when the spatial distribution is flat. The Galactic center proper motion data cited above [63] suggest approximate isotropy in the (projected) inner parsec. Theoretically, two-body encounters should drive the distribution toward isotropy near the SMBh while at the same time populating the low-angular-momentum orbits, pro-

ducing an isotropic density cusp. However since the cusp is not observed, it is not clear that relaxation has had sufficient time to reduce anisotropies to low values [47]. We therefore considered non-zero values of β even when setting $\gamma = 1$ or 2.

The following distribution of orbital elements:

$$N(a, e^2) da de^2 = N_0 g(a) h(e^2) da de^2, \quad (34a)$$

$$g(a) = a^{2-\gamma}, \quad (34b)$$

$$h(e^2) = (1 - e^2)^{-\beta}, \quad \beta \leq \gamma - 1/2 \quad (34c)$$

generates steady-state phase-space distributions with the properties defined above. Monte-Carlo realizations of the stellar positions and velocities were generated from this expression given the parameters $(\gamma, \beta, \tilde{M}_{\star}, \mathcal{R})$. Relativistic corrections were ignored when generating the initial conditions. We assumed that $N(a, e^2) = 0$ for $a > a_{\max}$; in most of the simulations, $a_{\max} = 4$ mpc, but smaller values were adopted as necessary to limit the total number of particles to ~ 180 , since for larger N the ARCHAIN routine was found to run very slowly. Table I gives the composition of all the models discussed below.

Stellar orbits were excluded from the initial conditions if their periaapse fell below $20GM_{\bullet}/c^2$, roughly the distance at which a solar-mass star on the main sequence would be tidally disrupted.

For each set of parameters defining the initial distribution, a set of different Monte-Carlo realizations was generated and independently integrated forward in time. The number N_{rand} of independent realizations was chosen such that the total number of MS stars in the combined set of integrations was $\gtrsim 10^3$. In addition, some integrations were repeated with the masses of the MS stars and BHs set to zero (leaving just the relativistic terms capable of inducing evolution of the orbital planes); and with the SBH spin set to zero (leaving just the Newtonian perturbations).

Given these models for the stellar cluster, we can use Eq. (29) to compute the approximate radii r_{crit} where frame-dragging begins to dominate stellar perturbations. Assuming that the density is dominated either by $1M_{\odot}$ MS stars ($\mathcal{R} \ll 1$) or by $10M_{\odot}$ BHs ($\mathcal{R} \gtrsim 1$), we find:

$$\tilde{r}_{\text{crit}} \approx \left[\frac{(43, 14)\chi}{(1 - e^2)^{3/2} \tilde{M}_{\star}^{1/2}} \right]^{\frac{2}{6-\gamma}} \text{ mpc} \quad (35)$$

where the first number in parentheses refers to the MS cluster and the second to the BH cluster. Fig. 3 plots r_{crit} vs. \tilde{M}_{\star} for various values of χ assuming $e = 2/3$, the mean eccentricity in an isotropic distribution.

V. RESULTS

In the N -body simulations, we characterized changes in stellar orbital orientations in two ways: via $\Delta\Omega$, the change in the nodal angle (defined with respect

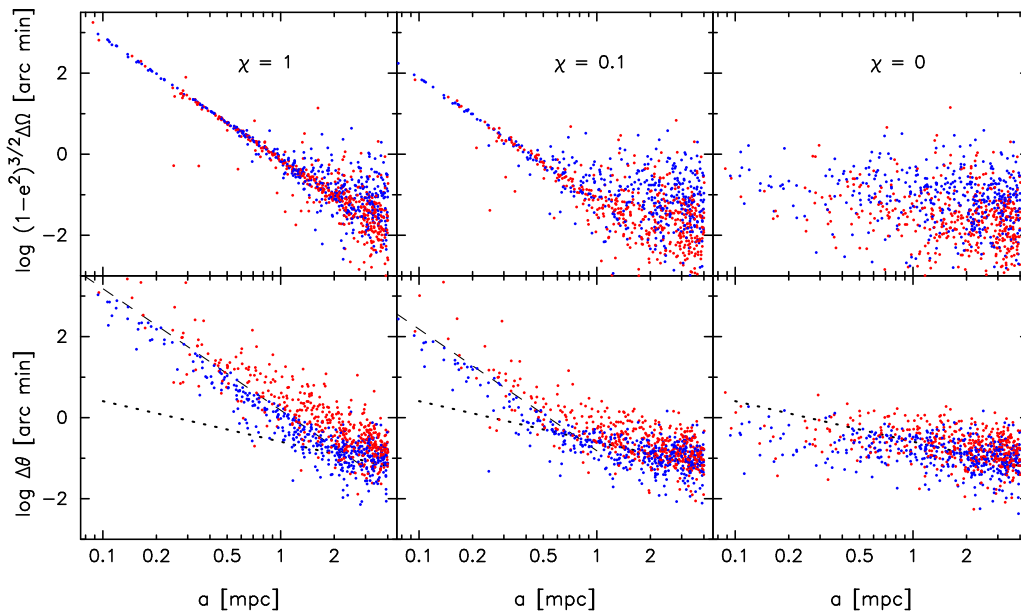


FIG. 4: Changes over 10 years in the orientations of stellar orbital planes, as measured via $\Delta\Omega$ (top) and $\Delta\theta$ (bottom). Parameters of the N -body models were $\gamma = 2$, $\beta = 0$, $\mathcal{R} = 1$, and $M_\star = 30M_\odot$ ($N_{\text{MS}} = 10$, $N_{\text{BH}} = 11$). Each point corresponds to a single star in a single integration; red points are orbits with initial eccentricities $0.7 < e \leq 1$ and blue points have $0 \leq e \leq 0.7$. In the lower panels, dashed lines show Eq. (24), the frame-dragging precession, for $e = 2/3$, and dotted lines show Eq. (27), the approximate model for precession due to stellar perturbations.

to the SBH equatorial plane); and via the coordinate-independent quantity $\Delta\theta$, the angle between the initial and final orbital angular momentum vectors (Eq. 17). The nodal angle advances uniformly in time in response to GR effects (Eq. 8); furthermore for a given χ and Δt , the quantity $(1 - e^2)^{3/2} \Delta\Omega$ depends only on a in the frame-dragging regime (Eq. 6b, 8).

Fig. 4 plots $(1 - e^2)^{3/2} \Delta\Omega$ and $\Delta\theta$ vs. a for each of the MS stars in a set of 10-year integrations of models with $\gamma = 2$, $\beta = 0$, $\mathcal{R} = 1$ and $\tilde{M}_\star = 30$ and three different values of the SBH spin, $\chi = (1, 0.1, 0)$. Also shown are the predicted, rms values of $\Delta\theta$ from Eqs. (24) (frame dragging) and (27) (stellar perturbations). In this model cluster, in which stellar BHs dominate the total mass, stellar perturbations dominate changes due to frame-dragging beyond radii of $\sim 1(0.3)$ mpc for $\chi = 1(0.1)$. As measured via $\Delta\theta$, GR effects are strongest for eccentric orbits, as expected, while the amplitude of the stellar perturbations is not noticeably e -dependent. The stellar perturbation model derived above is reasonably good at predicting the mean value of $\Delta\theta$ in the integration with $\chi = 0$, although the observed dependence on a appears to be shallower than predicted for $a \lesssim 0.5$ mpc.

Because of the large scatter in the amplitude of stellar perturbations at each a , the radius at which the GR signal clearly stands out from the “noise” is somewhat smaller than would be predicted from the rms values alone (Fig. 3).

The dependence of these results on the amount of distributed mass is shown in Fig. 5, which summa-

rizes results from integrations of models with $M_\star = (10, 30, 100)M_\odot$; other parameters are as in Fig. 4. As M_\star is increased, the amplitude of the “noise” from star-star perturbations increases, roughly in proportion to M_\star . These plots also indicate the expected amplitude of the quadrupole-induced precession. For $\chi = 1$, stellar perturbations dominate changes due to the quadrupole at radii beyond $\sim 0.5(0.3)$ mpc for $M_\star = 10(100)M_\odot$.

Fig. 6 shows the results of a comprehensive set of integrations using different models for the stellar cluster (Table 1). Especially when the SBH spin is low ($\chi = 0.1$), stellar perturbations can dominate the signal due to frame-dragging down to very small distances from the SBH, e.g. ~ 0.2 mpc for $\tilde{M}_\star = 100$, corresponding to orbital periods of ~ 0.1 yr.

We define the “astrometric precessions” $\Delta\Theta \equiv (a/D)\Delta\theta$ where $D = 8.0$ kpc is the distance to the Galactic center [1]. $\Delta\Theta$ is roughly the angular displacement of the orbital axes, as seen from the Earth (ignoring projection effects).

In the following section we discuss how measurements of \mathbf{J} and \mathbf{Q} might be feasible even in cases where the stellar perturbations are significant. Here, we assume that, in order to be useful for tests of GR, a star must satisfy two minimum conditions:

- 1 Its astrometric precession must exceed some minimum threshold set by the detector.
- 2 Its precession must be dominated by GR effects.

We call MS stars that satisfy both conditions “detectable.”

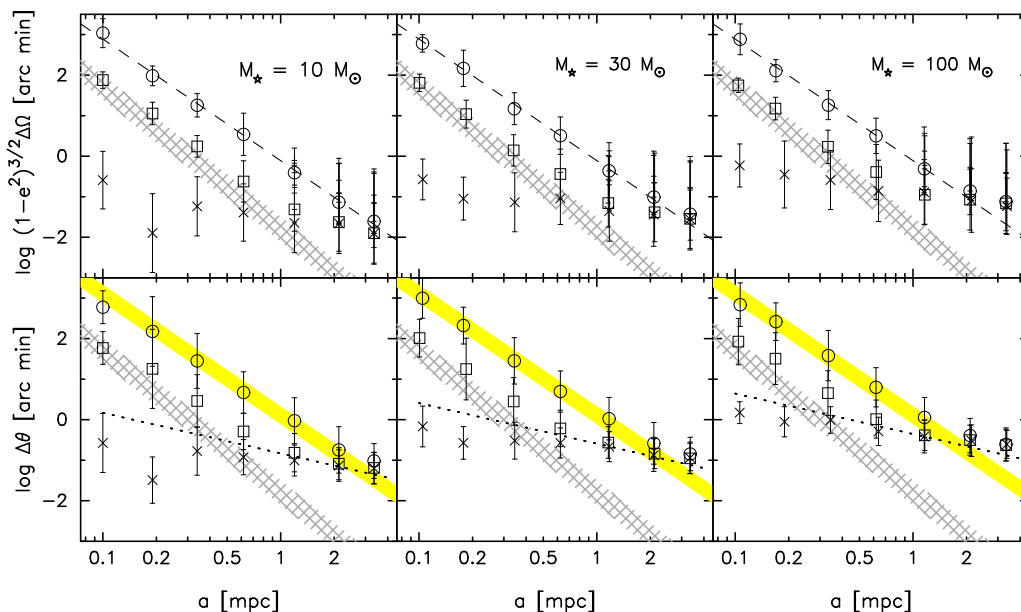


FIG. 5: Similar to Fig. 4 except that average values have been computed in bins of semi-major axis. Three different N -body models are shown, differing in the distributed mass: $M_* = (10, 30, 100)\mathcal{M}_\odot$. All models have $\gamma = 2$, $\beta = 0$, $\mathcal{R} = 1$ as in Fig. 4. Open circles: $\chi = 1$; squares: $\chi = 0.1$; crosses: $\chi = 0$. The predicted angular changes for $\chi = 1$ due to frame-dragging are shown as the dashed lines in the upper histograms and as the yellow band in the lower histograms. The cross-hatched regions indicate the range of precession amplitudes expected from the SBH quadrupole moment alone. Dotted lines in the lower frames are the approximate model for stellar perturbations, Eq. (27).

We base our assumptions about the minimum observable angular changes on the specifications for the planned instrument GRAVITY [23]. GRAVITY will observe the Galactic center three times a year (in April, July and September) and the error in each astrometric data point will be $\delta\Theta \approx 10\mu\text{as}$ (F. Eisenhauer, private communication). Since the precession is linear with respect to time, the uncertainty in the measured astrometric precession after n observations is

$$\sigma_{\Delta\Theta} \approx 2\sqrt{3}\sqrt{\frac{n-1}{n(n+1)}}\delta\Theta \approx 35\mu\text{as}\sqrt{\frac{n-1}{n(n+1)}}. \quad (36)$$

For an elapsed time of $1(3)10$ yr, $\sigma_{\Delta\Theta} = 14(10)6.2\mu\text{as}$.

Fig. 7 plots the distribution of $\Delta\Theta$ values after 10 years due to star-star perturbations in one model, $(\gamma, \beta, \bar{M}_*) = (2, 0, 30)$. Also plotted are the distributions that would arise from frame-dragging and quadrupole torques alone, $\Delta\Theta_{J,Q} = (a/D)\Delta\Omega_{J,Q}\sin i$ (cf. Eq. 20), for the same stars. Fig. 7 suggests that a clean separation of frame-dragging and Newtonian precessions for most stars in this model requires $a \lesssim 0.5$ mpc for $\chi = 1$ and $a \lesssim 0.2$ mpc for $\chi = 0.1$. For these values of a the amplitude of $\Delta\Theta_J$ is greater than $10\mu\text{as}$ for most stars, making them accessible to astrometric monitoring. High eccentricities, $e \gtrsim 0.9$, allow these requirements to be relaxed: eccentric orbits with a as large as $\sim 1(0.5)$ mpc can produce measurable displacements that are significantly greater than those due to stellar perturbations.

Detecting the effects of the quadrupole moment in this model would be considerably harder. For $\chi = 1$, the

quadrupole precessions separate cleanly from the stellar perturbations only for $a \lesssim 0.1$ mpc, or $a \lesssim 0.3$ for the most eccentric stars.

Regardless of the number of stars that satisfy conditions 1 and 2, an additional requirement is that

- 3 the stars satisfying these conditions must constitute a large fraction of *all* stars in the region being observed

since otherwise there is a large probability that the precession of a randomly-chosen star will be dominated by non-GR effects.

We calculated the average number of detectable stars, $\langle N_{\text{detect}} \rangle$, in each of our models after expressing conditions 1 and 2 in the forms

- 1 $\Delta\Theta > \sigma_{\Delta\Theta}$
- 2 $\Delta\Theta_{J,Q} > \Delta\Theta_{95}$

where $\Delta\Theta_{95}$ is the upper edge of the 95% confidence interval of the distribution of stellar perturbations. Observational intervals of $\Delta t = (1, 3, 10)$ yr were considered.

The results are shown in Figs. 8 and 9 for four models of the stellar cluster, and in four bins of semi-major axis. The figures also show f , the ratio of $\langle N_{\text{detect}} \rangle$ to the total number of stars in each bin, and $\langle \Delta\Omega \rangle$, the average value of the ‘‘astrometric precession’’ for the detectable stars. $\langle N_{\text{detect}} \rangle \gtrsim 1$ means that at least one star would be expected to be present that satisfies the two detectability criteria; if in addition f is large, such stars constitute a large fraction of all stars in the same radial bin.

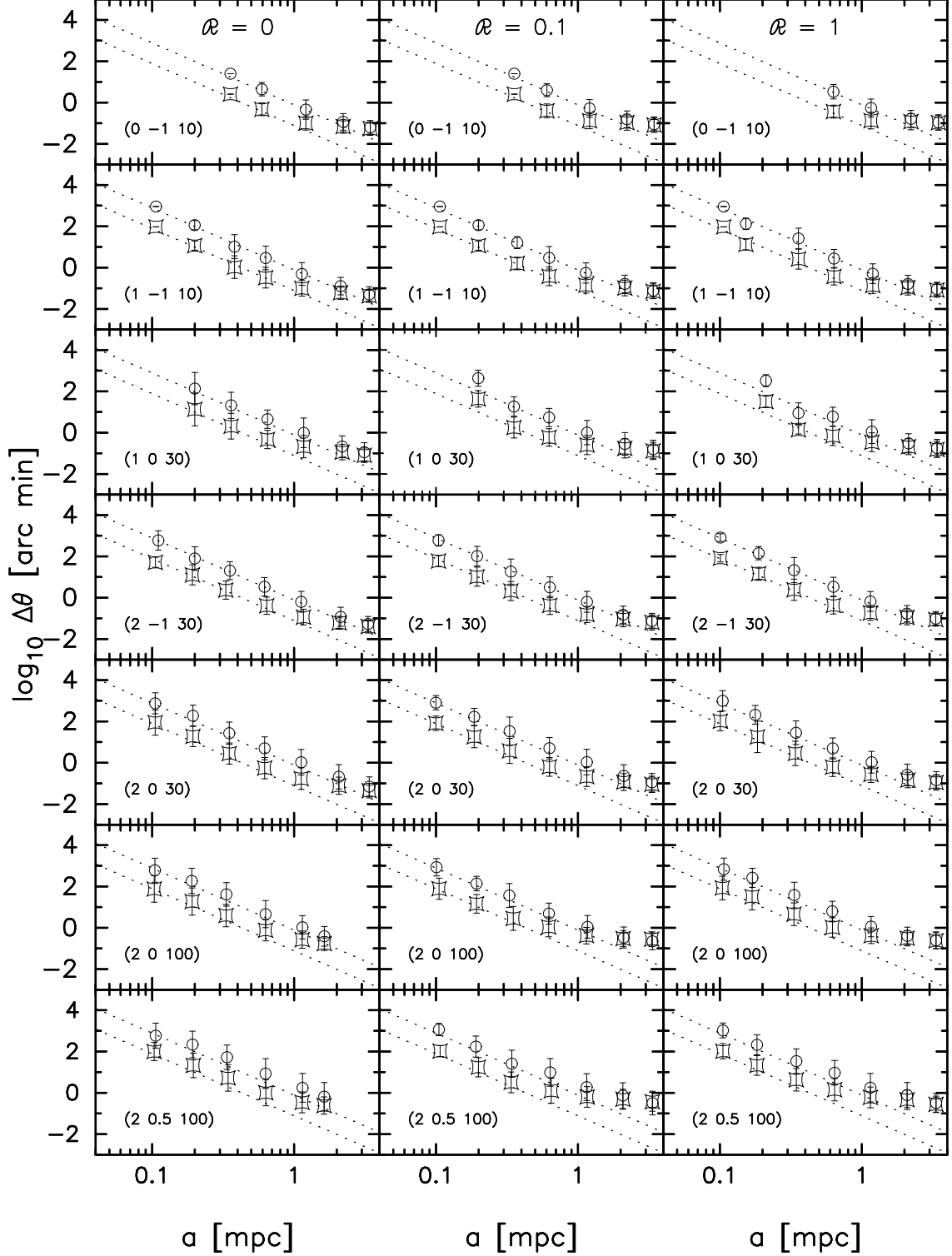


FIG. 6: Changes over 10 years in the orientation of stellar orbital angular momentum vectors, in N -body integrations of various models (Table 1). The three columns correspond to three values $\mathcal{R} = (0, 0.1, 1)$ of the ratio of BHs to MS stars; the values of γ, β and \tilde{M}_* that characterize the stellar distribution are given in the lower left of each panel. Circles are for integrations with $\chi = 1$ and squares are for $\chi = 0.1$. Dashed lines show the expected, rms contribution to $\Delta\theta$ from frame dragging for both values of χ .

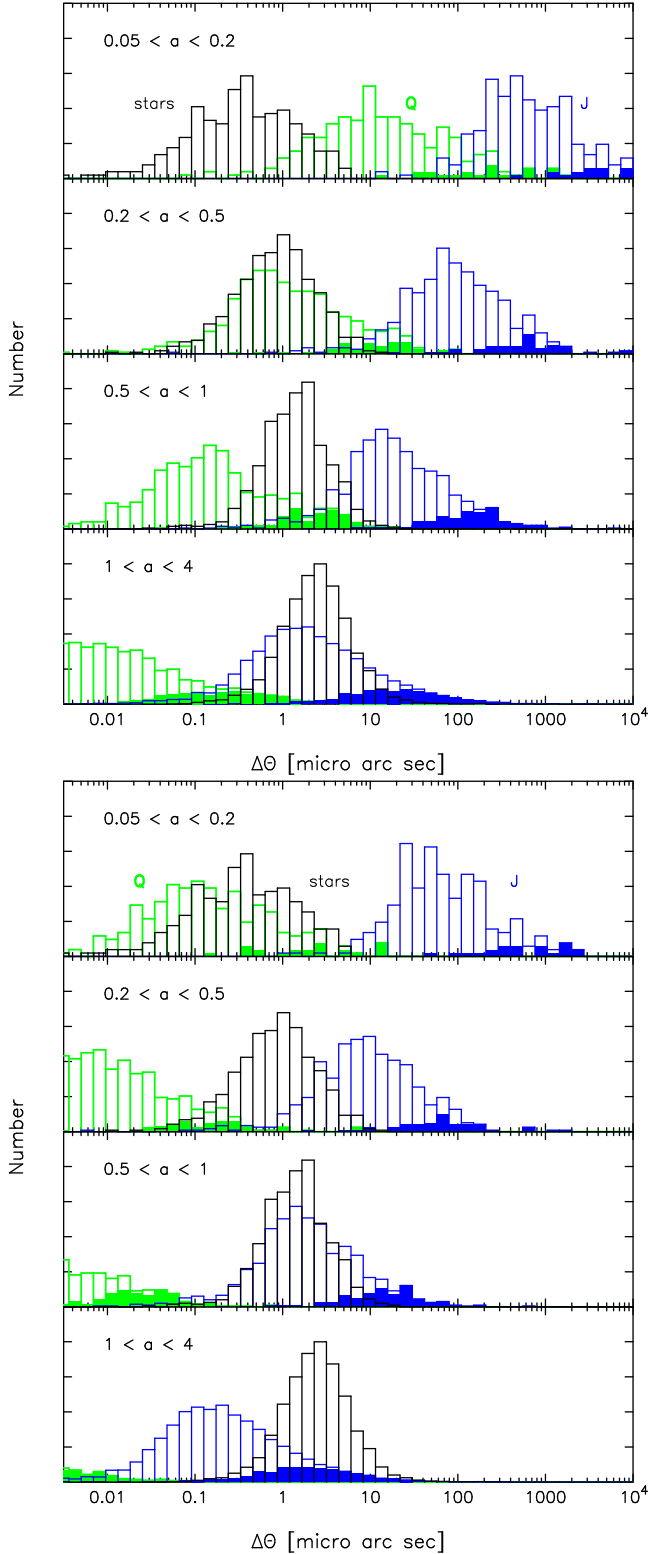


FIG. 7: “Astrometric” precessions of orbital planes over 10 years, based on integrations of the model with $(\gamma, \beta, \tilde{M}_*) = (2, 0, 30)$. Black histograms are from integrations in which the SBH spin was set to zero (although non-spin PN terms were included) and show the effects of stellar perturbations. Blue histograms are the predicted precessions due to frame-dragging alone for the same stars; filled bars are stars with $e \geq 0.9$. Green histograms show the predicted precessions due to the SBH quadrupole moment alone, again with high- e orbits indicated. The assumed value of the SBH spin is $\chi = 1$ in the top frames and $\chi = 0.1$ in the bottom frames.

The figures illustrate the tradeoff that occurs between the number of detectable stars at a given radius, and the certainty that a single star at that radius is responding to GR effects rather than to stellar perturbations. For example, going across the second column in Fig. 8 (i.e. $\gamma = 1, \beta = 0, \tilde{M}_* = 30$), $\langle N \rangle$ increases steadily with increasing a , but f behaves oppositely, dropping below 10% in most cases for $a \gtrsim 1$ mpc.

With regard to frame dragging Fig. 8 suggests the following.

- In models with low central densities, $\gamma = (0, 1)$, detection of frame-dragging precession may be feasible after $\Delta t \gtrsim 3$ yr for orbits with $0.2 \lesssim a/\text{mpc} \lesssim 1$. At smaller radii the number of stars is too small; at larger radii the noise from stellar perturbations is too great.
- In models with a steep density profile, $\gamma = 2$, detection of frame dragging is feasible at $a \leq 0.2$ mpc after $\Delta t = 1$ yr in most of the models; at $a \leq 0.5$ mpc after $\Delta t = 3$ yr; and at $a \leq 1$ mpc after $\Delta t = 10$ yr. The exceptions are models with a large fraction of stellar BHs ($\mathcal{R}=1$) in which the stellar perturbations always dominate.

With regard to quadrupole precession, Fig. 9 suggests that $\langle N_{\text{detect}} \rangle > 1$ occurs in tandem with large ($\gtrsim 50\%$) f only for rather narrow sets of parameters, e.g. $\gamma \approx 2, \tilde{M} \approx 30, a \lesssim 0.2 \text{ mpc}, \mathcal{R} \lesssim 0.1, \Delta t \gtrsim 10$ yr. Detecting the effects of the quadrupole torque above noise from the stellar perturbations is apparently only feasible if the stellar cluster is rather finely tuned: there must be a substantial number of stars very close to the SBH, $r \lesssim 0.2$ mpc, but at the same time a small number of stellar remnants so that the stellar perturbations do not dominate.

In practice, the quadrupole-induced precession may be large compared with that due to stellar perturbations, but still small compared with precession due to frame dragging, making it difficult to see in the data. As shown in Fig. 1, $t_Q < t_J$ only holds at very small radii, $r \lesssim 0.05$ mpc, unless eccentricities are large.

VI. DISCUSSION

A. Compensating for stellar perturbations

The numerical experiments described above were designed to elucidate the extent to which “noise” from stellar perturbations can mask the signal from GR spin effects at the Galactic center. In situations where the stellar perturbations are present but not dominant, one would like to be able to detect the perturbations and remove their effects from the data. Here we outline one approach to that problem.

Suppose that one observes a set of stars at the discrete times $t_j, j = 1, \dots, N_{\text{obs}}$. Denoting the stars by index

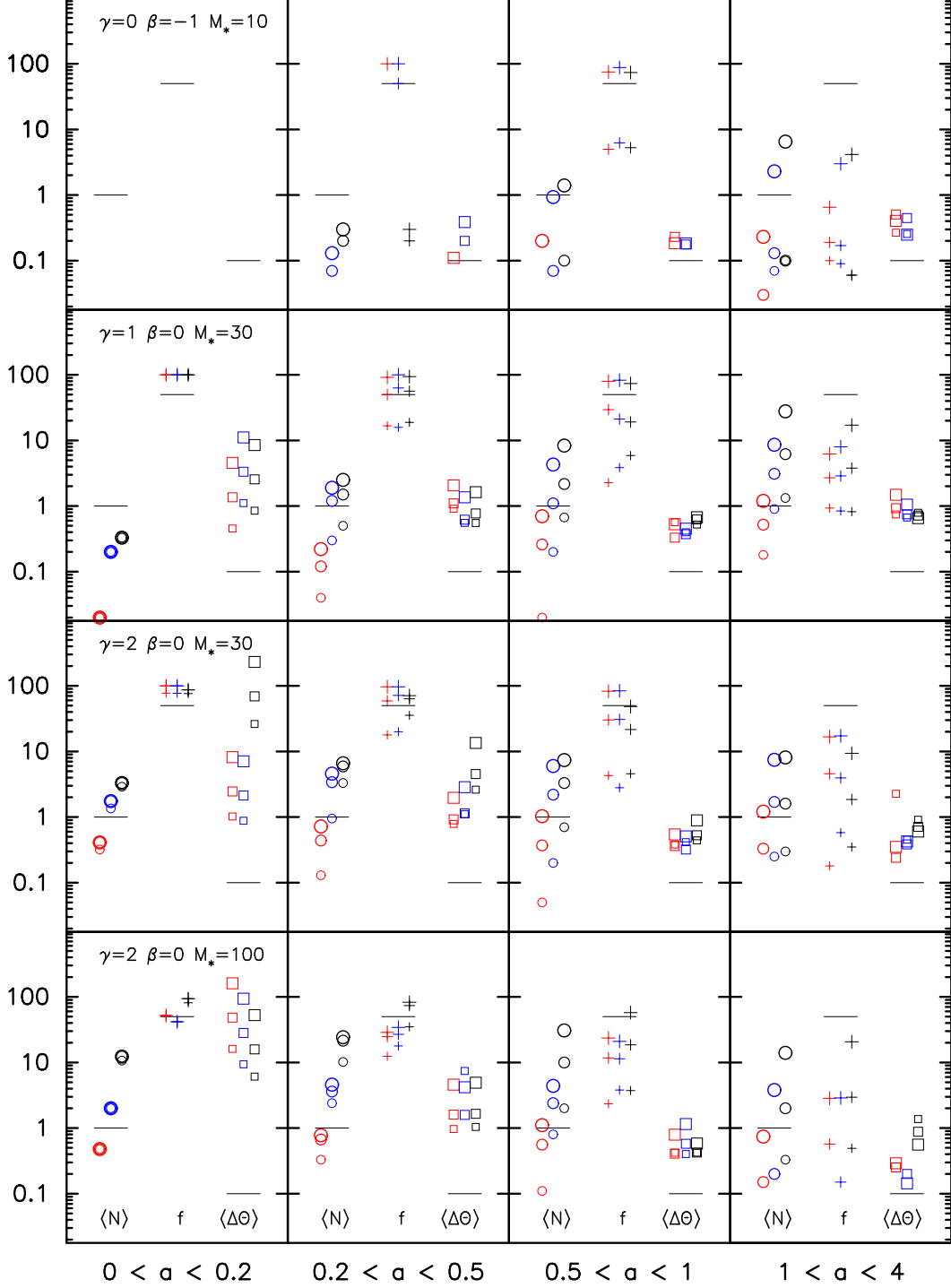


FIG. 8: Detectability of frame-dragging in four models for the stellar cluster. Results are displayed in four bins of semi-major axis a (in mpc). In each panel, circles denote $\langle N_{\text{detect}} \rangle$, the average number of stars with detectable precessions, as defined in the text; + symbols denote the percentage of stars that are detectable in that bin; and \square symbols denote the average precession angle of the detectable stars in the bin, expressed in units of 10^{-4} arc min. In each group of similar symbols, the left (red), middle (blue) and right (black) symbols are for models with $\mathcal{R} = (1, 0.1, 0)$ respectively, while the integration time is indicated by the size of the symbol: 1 yr (smallest), 3 yr, and 10 yr (biggest). The tick marks indicate $\langle N_{\text{detect}} \rangle = 1$, $f = 50\%$, and $\langle \Delta\theta \rangle = 10\mu\text{as}$.

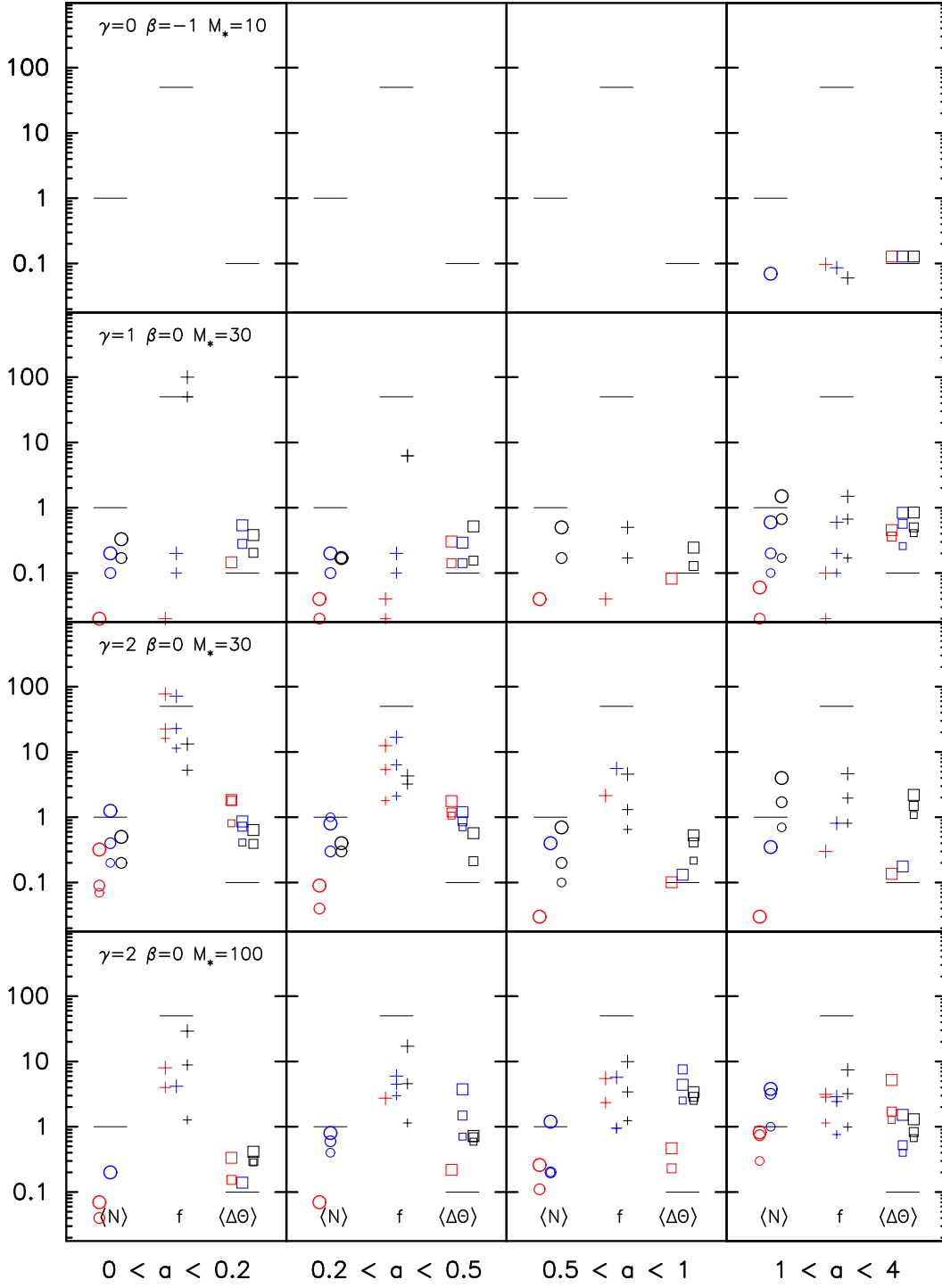


FIG. 9: Detectability of quadrupole precession. All symbols are defined as in Fig. 8.

$k = 1, \dots, N_{\text{orb}}$, the N_{orb} orbital solutions are required to satisfy the equations

$$\frac{d\mathbf{L}_k}{dt} = \boldsymbol{\omega}_k \times \mathbf{L}_k(t_j) + \mathbf{r}(t_j) \times \mathbf{F}_N(t_j, \mathbf{r}), \quad (37a)$$

$$\boldsymbol{\omega}_k = P_k^{-1} (A_{J,k} - A_{Q,k} \cos i_k) \hat{\mathbf{J}} \quad (37b)$$

Here $\mathbf{F}_N(t, \mathbf{r})$ is the perturbing force field due to all the

stars and stellar remnants, and $\mathbf{r}_k(t)$ is the position of the k th star at time t_j . \mathbf{F}_N depends explicitly on the time, to the extent that the orbits of the stars that produce the perturbing force are changing.

We first consider the orbital solutions for each observed star separately. In their most general form, equations (37) are under-determined ($3N_{\text{obs}}$ equations with

$3 + 3N_{\text{obs}}$ unknowns). To make progress, it is necessary to introduce approximations. On the short time scales of relevance, the contribution to the total gravitational potential from the stars can be considered (1) fixed in time and (2) not strongly varying in space. For instance, a spatially uniform \mathbf{F} is the lowest order term in a multipole expansion, and one could add, if necessary, dipole and quadrupole terms, etc.

As an example, we consider a stellar perturbation that is modeled as

$$\Phi_*(x, y, z) = 2\pi G \rho_t (A_x x^2 + A_y y^2 + A_z z^2). \quad (38)$$

This is the potential due to a homogeneous triaxial cluster centered on the SBH and aligned with the coordinate axes; the dimensionless quantities (A_x, A_y, A_z) are determined by the axis ratios of the ellipsoid [64]. Proceeding as in the derivation of Eq. (8), one can derive the (Newtonian) orbit-averaged effect of this perturbing potential on the orientations of orbital planes. For instance, in the case of low-eccentricity orbits, one finds [65]

$$\frac{d\mathbf{L}}{dt} = \mathbf{T}_N, \quad (39a)$$

$$\mathbf{T}_N = \frac{4\pi G \rho_t a^2}{L^2} \begin{pmatrix} (A_z - A_x)L_y L_z \\ (A_y - A_z)L_x L_z \\ (A_x - A_y)L_x L_y \end{pmatrix} \quad (39b)$$

with L constant. Similar expressions can be derived for orbits of arbitrary eccentricity [65].

In practice, one would simultaneously fit all the parameters appearing in Eq. (37) to the observed positions and/or velocities. In the case of the model potential just assumed, this would amount to introducing 9 additional parameters to the 6 required for a Keplerian solution, i.e. ω_k ; the perturbing density ρ_t and its two axis ratios; and the three direction cosines that define the orientation of the ellipsoid. A data set with $N_{\text{obs}} \geq 5$ is then formally well-determined. Note however that $N_{\text{obs}} \gg 5$ is required to obtain a full solution with a reasonable goodness-of-fit. Repeating this fitting procedure for the N_{orb} orbits will then allow one to estimate the orbit-to-orbit variation in the parameters that define the perturbation. If the latter is large, the model can be made more general by the addition of extra parameters.

This fitting procedure will yield an estimate of ω_k for the N_{orb} orbits that is independent of any assumptions about the underlying physics of the GR precession, apart from the assumption that the precession rate is constant. Given enough orbits, the empirically determined values ω_k can be correlated with the orbital properties to test in an almost assumption-free way non-standard theories of gravity. The no-hair conjecture can be tested explicitly by substituting into equation (37b) the GR expressions (14):

$$\begin{aligned} A_{J,k} &= 4\pi\chi\varrho_k^{-3/2}, \\ A_{Q,k} &= 3\pi\chi^2\varrho_k^{-2} \end{aligned} \quad (40)$$

with ϱ the penetration parameter defined above. The torque equation (37) can then be written as

$$\begin{aligned} \frac{d\mathbf{L}_k}{dt} &= 4\pi \left(\varrho_k^{-3/2}/P_k \right) \\ &\left[1 + \frac{3}{4}\varrho_k^{-1/2}\boldsymbol{\chi} \cdot (\mathbf{L}_k/L_k) \right] (\boldsymbol{\chi} \times \mathbf{L}_k) + \mathbf{T}_{N,k} \end{aligned} \quad (41)$$

The second (small) term in the square brackets ($\varrho_k \gg 1$) reflects the relative contribution of the quadrupole moment to the precession. The same fitting procedure outlined above for the general case can be carried out here, with the difference that the vector $\boldsymbol{\chi}$, which replaces $\boldsymbol{\omega}_k$, is common to all the orbits, and therefore a simultaneous fitting of the entire set of N_{orb} orbits will improve the power of the orbital solutions. The comparison of the best fit values of $\boldsymbol{\chi}$ from individual orbits to the one from the simultaneous global fit can help assess the robustness of the result.

An initial test of the no-hair conjecture could be obtained by repeating the fit once with, and once without the quadrupole term, to check whether the quadrupole term indeed improves the fit. A slightly more discriminating test would be to introduce an extra free pre-factor f_Q to the quadrupole term, and see whether the best fit yields $f_Q \sim 1$. More sophisticated tests would require assuming specific alternative functional forms for the quadrupole term.

B. Independent constraints on the spin

The foregoing assumes that the mass M_\bullet of the Milky Way SBH is a known quantity, i.e. that it need not be treated as a free parameter when fitting the astrometric data to Eq. (37). Determinations of M_\bullet are based on the motion of stars on spatial scales of $10^1 - 10^3$ mpc [9, 10, 63], outside the region where GR spin effects are detectable.

In the same way, independent measurements of the magnitude and direction of the SBH's spin \mathbf{J} could remove as many as three additional parameters from Eq. (37), reducing the uncertainty on estimates of the quadrupole moment.

A number of approaches to the determination of \mathbf{J} are being pursued. Sgr A*, the compact source of radio, infrared and X-radiation at the center of the Milky Way, exhibits variability at IR and X-ray wavelengths on time scales as short as 20 – 30 minutes that can be interpreted as emission from “hot spots” in orbits just outside the SBH event horizon [66, 67, 68, 69]. If this interpretation is correct, $\chi \gtrsim 0.3 - 0.5$ is required in order that the orbital period at the innermost stable orbit be as short as the observed rise times for the flaring events [66, 70, 71]. Very long baseline interferometry at sub-mm wavelengths has the capacity to resolve the structure of the plasma surrounding the SBH on angular scales of 10 – 100 μas , comparable to r_g [72, 73]. Such observa-

tions can constrain the spin via comparison with theoretical accretion disk models, or by detection of variability on spatial scales of $\sim r_g$ [74, 75, 76]. The properties of the X-ray polarization from the inner accretion disk are also predicted to be spin-dependent [77].

Constraints on \mathbf{J} derived from observations like these will be highly model-dependent, requiring assumptions about the nature of the emission, the geometry and physical state of the emitting gas (accretion vs. outflow or jets), etc. It is not clear at present whether the systematic uncertainties of these independent spin measurements will be larger or smaller than the uncertainties associated with astrometric estimates of the spin; the latter are due both to the stellar perturbations modelled here, and also to the difficulties associated with measurement of proper motions of faint stars in crowded fields [27]. Additional, if uncertain, information on the SBH spin can be used to improve the global orbital solutions by including it as prior probabilities in Bayesian best-fit methods for large-dimensional parameter spaces, such as the Markov Chain Monte Carlo method [78, 79].

VII. CONCLUSIONS

1. The spin and quadrupole moment of the Galactic center supermassive black hole (SBH) can in principle be measured by observing the precession of the orbital planes of stars in the inner milliparsec (mpc) [1]. However, gravitational interactions between stars in this region are likely to induce orbital precession of the same approximate amplitude as the precession due to frame dragging. The stellar perturbations manifest themselves as coherent torques over short time scales, mimicking general relativistic (GR) precession.
2. The number of stars and stellar remnants (e.g. stellar-mass black holes, BHs) in this region is uncertain, but small enough ($\sim 10^0 - 10^3$) that full N -body simulations are feasible. A regularized post-Newtonian N -body algorithm is presented that includes the lowest-order spin-

orbit and quadrupole-orbit terms.

3. Assuming near-maximal spin for the Milky Way SBH, detection of frame-dragging precession may be feasible after a few years' monitoring with an instrument like GRAVITY [23] for orbits in the radial range between ~ 0.2 mpc and ~ 1 mpc. At smaller radii the number of stars is too small, while at larger radii the star-star and star-remnant perturbations dominate GR effects. In models where the number of stellar BHs is comparable to the number of observable stars, GR effects are almost always swamped by perturbations from the remnants.
4. Quadrupole-induced precession stands out clearly from stellar perturbations only in a narrow class of models for the nuclear star cluster, having moderate to high central densities and a small BH fraction, and only at radii $r \lesssim 0.2$ mpc.
5. Because the orbit-averaged torques from stars are approximately constant in magnitude over year-long time scales, it is possible in principle to disentangle the effects of stellar perturbations from those due to GR, allowing tests of gravity even in the presence of stellar perturbations.

Acknowledgments

DM was supported in part by the National Science Foundation under grants no. AST 08-07910, 08-21141 and by the National Aeronautics and Space Administration under grant no. NNX-07AH15G. TA was supported by ISF grant no. 928/06 and by ERC Starting Grant 202996. CMW was supported in part by the National Science Foundation under grant no. PHY 06-52448 and the National Aeronautics and Space Administration under grant no. NNG-06GI60G. CMW is grateful for the hospitality of the Institut d'Astrophysique de Paris where parts of this research were carried out. We thank H. Bartko, F. Eisenhauer and S. Noble for useful discussions.

-
- [1] C. M. Will, *Astrophys. J. Letts.* **674**, L25 (2008).
 - [2] A. Krabbe, R. Genzel, A. Eckart, F. Najarro, D. Lutz, M. Cameron, H. Kroker, L. E. Tacconi-Garman, N. Thatte, L. Weitzel, et al., *Astrophys. J. Lett.* **447**, L95+ (1995).
 - [3] R. D. Blum, K. Sellgren, and D. L. Depoy, *Astron. J.* **112**, 1988 (1996).
 - [4] D. F. Figier, E. E. Becklin, I. S. McLean, A. M. Gilbert, J. R. Graham, J. E. Larkin, N. A. Levenson, H. I. Teplitz, M. K. Wilcox, and M. Morris, *Astrophys. J. Letts.* **533**, L49 (2000).
 - [5] S. Gezari, A. M. Ghez, E. E. Becklin, J. Larkin, I. S. McLean, and M. Morris, *Astrophys. J.* **576**, 790 (2002).
 - [6] T. Paumard, R. Genzel, F. Martins, S. Nayakshin, A. M. Beloborodov, Y. Levin, S. Trippe, F. Eisenhauer, T. Ott, S. Gillessen, et al., *Astrophys. J.* **643**, 1011 (2006).
 - [7] Q. Zhu, R. P. Kudritzki, D. F. Figier, F. Najarro, and D. Merritt, *Astrophys. J.* **681**, 1254 (2008).
 - [8] A. M. Ghez, S. Salim, S. D. Hornstein, A. Tanner, J. R. Lu, M. Morris, E. E. Becklin, and G. Duchêne, *Astrophys. J.* **620**, 744 (2005).
 - [9] A. M. Ghez, S. Salim, N. N. Weinberg, J. R. Lu, T. Do, J. K. Dunn, K. Matthews, M. R. Morris, S. Yelda, E. E. Becklin, et al., *Astrophys. J.* **689**, 1044 (2008).
 - [10] S. Gillessen, F. Eisenhauer, S. Trippe, T. Alexander, R. Genzel, F. Martins, and T. Ott, *Astrophys. J.* **692**, 1075 (2009).
 - [11] R. Schödel, T. Ott, R. Genzel, R. Hofmann, M. Lehnert, A. Eckart, N. Mouawad, T. Alexander, M. J. Reid, R. Lenzen, et al., *Nature (London)* **419**, 694 (2002).

- [12] A. M. Ghez, G. Duchêne, K. Matthews, S. D. Hornstein, A. Tanner, J. Larkin, M. Morris, E. E. Becklin, S. Salim, T. Kremenek, et al., *Astrophys. J. Letts.* **586**, L127 (2003).
- [13] M. J. Reid, *Ann. Rev. Astron. Astrophys.* **31**, 345 (1993).
- [14] F. Eisenhauer, R. Genzel, T. Alexander, R. Abuter, T. Paumard, T. Ott, A. Gilbert, S. Gillessen, M. Horrobin, S. Trippe, et al., *Astrophys. J.* **628**, 246 (2005).
- [15] M. A. T. Groenewegen, A. Udalski, and G. Bono, *Astron. Astrophys.* **481**, 441 (2008).
- [16] S. Gillessen, F. Eisenhauer, T. K. Fritz, H. Bartko, K. Dodds-Eden, O. Pfuhl, T. Ott, and R. Genzel, *ArXiv e-prints* (2009), 0910.3069.
- [17] M. Jaroszynski, *Acta Astronomica* **48**, 653 (1998).
- [18] P. C. Fragile and G. J. Mathews, *Astrophys. J.* **542**, 328 (2000).
- [19] N. N. Weinberg, M. Milosavljević, and A. M. Ghez, *Astrophys. J.* **622**, 878 (2005).
- [20] S. Zucker, T. Alexander, S. Gillessen, F. Eisenhauer, and R. Genzel, *Astrophys. J. Letters* **639**, L21 (2006).
- [21] G. F. Rubilar and A. Eckart, *Astron. Astrophys.* **374**, 95 (2001).
- [22] A. F. Zakharov, A. A. Nucita, F. de Paolis, and G. Ingrassio, *Phys. Rev. D* **76**, 062001 (2007).
- [23] F. Eisenhauer, G. Perrin, W. Brandner, C. Straubmeier, A. Böhm, H. Baumeister, F. Cassaing, Y. Clénet, K. Dodds-Eden, A. Eckart, et al., in *Science with the VLT in the ELT Era*, edited by A. Moorwood (2009), pp. 361–+.
- [24] J. Pott, J. Woillez, P. L. Wizinowich, A. Eckart, A. Glindemann, A. M. Ghez, and J. R. Graham, in *Society of Photo-Optical Instrumentation Engineers (SPIE) Conference Series* (2008), vol. 7013 of *Presented at the Society of Photo-Optical Instrumentation Engineers (SPIE) Conference*.
- [25] R. Kannan and P. Saha, *Astrophys. J.* **690**, 1553 (2009).
- [26] M. Preto and P. Saha, *Astrophys. J.* **703**, 1743 (2009).
- [27] T. Fritz, S. Gillessen, S. Trippe, T. Ott, H. Bartko, O. Pfuhl, K. Dodds-Eden, R. Davies, F. Eisenhauer, and R. Genzel, *Mon. Not. R. Astron. Soc.* pp. 1578–+ (2009), 0909.2592.
- [28] J. Lense and H. Thirring, *Physikalische Zeitschrift* **19**, 156 (1918).
- [29] D. C. Wilkins, *Phys. Rev. D* **5**, 814 (1972).
- [30] D. Merritt and E. Vasiliev (2010), in preparation.
- [31] K. P. Rauch and S. Tremaine, *New Astro.* **1**, 149 (1996).
- [32] E. Eilon, G. Kupa, and T. Alexander, *Astrophys. J.* **698**, 641 (2009).
- [33] S. Mikkola and K. Tanikawa, *Celestial Mechanics and Dynamical Astronomy* **74**, 287 (1999).
- [34] S. Mikkola and K. Tanikawa, *Monthly Not. R. Astron. Soc.* **310**, 745 (1999).
- [35] S. Mikkola and S. J. Aarseth, *Celestial Mechanics and Dynamical Astronomy* **57**, 439 (1993).
- [36] S. Mikkola and S. Aarseth, *Celestial Mechanics and Dynamical Astronomy* **84**, 343 (2002).
- [37] S. Mikkola and D. Merritt, *Monthly Not. R. Astron. Soc.* **372**, 219 (2006).
- [38] S. Mikkola and D. Merritt, *Astron. J.* **135**, 2398 (2008).
- [39] M. H. Soffel, *Relativity in Astrometry, Celestial Mechanics and Geodesy* (Springer, 1989).
- [40] L. E. Kidder, *Phys. Rev. D* **52**, 821 (1995).
- [41] A. Eckart, R. Genzel, R. Hofmann, B. J. Sams, and L. E. Tacconi-Garman, *Astrophys. J. Lett.* **407**, L77 (1993).
- [42] R. Genzel, N. Thatte, A. Krabbe, H. Kroker, and L. E. Tacconi-Garman, *Astrophys. J.* **472**, 153 (1996).
- [43] R. M. Buchholz, R. Schödel, and A. Eckart, *Astron. Astrophys.* **499**, 483 (2009).
- [44] R. Genzel, R. Schödel, T. Ott, F. Eisenhauer, R. Hofmann, M. Lehnert, A. Eckart, T. Alexander, A. Sternberg, R. Lenzen, et al., *Astrophys. J.* **594**, 812 (2003).
- [45] T. Do, A. M. Ghez, M. R. Morris, J. R. Lu, K. Matthews, S. Yelda, and J. Larkin, *Astrophys. J.* **703**, 1323 (2009).
- [46] H. Bartko, F. Martins, S. Trippe, T. K. Fritz, R. Genzel, T. Ott, F. Eisenhauer, S. Gillessen, T. Paumard, T. Alexander, et al., *ArXiv e-prints* (2009), 0908.2177.
- [47] D. Merritt, *ArXiv e-prints* (2009), 0909.1318.
- [48] L. Spitzer, *Dynamical Evolution of Globular Clusters* (Princeton University Press, 1989).
- [49] J. N. Bahcall and R. A. Wolf, *Astrophys. J.* **209**, 214 (1976).
- [50] J. N. Bahcall and R. A. Wolf, *Astrophys. J.* **216**, 883 (1977).
- [51] T. Alexander, *Astrophys. J.* **527**, 835 (1999).
- [52] M. Freitag, P. Amaro-Seoane, and V. Kalogera, *Astrophys. J.* **649**, 91 (2006).
- [53] J. E. Dale, M. B. Davies, R. P. Church, and M. Freitag, *Mon. Not. R. Astron. Soc.* **393**, 1016 (2009), 0811.3111.
- [54] S. Nayakshin and R. Sunyaev, *Mon. Not. R. Astron. Soc.* **364**, L23 (2005).
- [55] H. Maness, F. Martins, S. Trippe, R. Genzel, J. R. Graham, C. Sheehy, M. Salaris, S. Gillessen, T. Alexander, T. Paumard, et al., *Astrophys. J.* **669**, 1024 (2007).
- [56] J. M. Scalo, *Fund. Cosmic Phys.* **11**, 1 (1986).
- [57] P. Kroupa, *Monthly Not. R. Astron. Soc.* **322**, 231 (2001).
- [58] M. Morris, *Astrophys. J.* **408**, 496 (1993).
- [59] C. Hopman and T. Alexander, *Astrophys. J. Lett.* **645**, L133 (2006).
- [60] T. Alexander and C. Hopman, *Astrophys. J.* **697**, 1861 (2009), 0808.3150.
- [61] D. Merritt and A. Szell, *Astrophys. J.* **648**, 890 (2006).
- [62] A. Eckart and R. Genzel, *Mon. Not. R. Astron. Soc.* **284**, 576 (1997).
- [63] R. Schödel, D. Merritt, and A. Eckart, *Astron. Ap.* **502**, 91 (2009).
- [64] S. Chandrasekhar, *Ellipsoidal figures of equilibrium* (1969).
- [65] N. Sambhus and S. Sridhar, *Astrophys. J.* **542**, 143 (2000).
- [66] R. Genzel, R. Schödel, T. Ott, A. Eckart, T. Alexander, F. Lacombe, D. Rouan, and B. Aschenbach, *Nature (London)* **425**, 934 (2003).
- [67] F. Yusef-Zadeh, D. Roberts, M. Wardle, C. O. Heinke, and G. C. Bower, *Astrophys. J.* **650**, 189 (2006).
- [68] A. Eckart, F. K. Baganoff, R. Schödel, M. Morris, R. Genzel, G. C. Bower, D. Marrone, J. M. Moran, T. Viehmann, M. W. Bautz, et al., *Astron. Ap.* **450**, 535 (2006).
- [69] D. P. Marrone, F. K. Baganoff, M. R. Morris, J. M. Moran, A. M. Ghez, S. D. Hornstein, C. D. Dowell, D. J. Muñoz, M. W. Bautz, G. R. Ricker, et al., *Astrophys. J.* **682**, 373 (2008).
- [70] G. Bélanger, R. Terrier, O. C. de Jager, A. Goldwurm, and F. Melia, *Journal of Physics Conference Series* **54**, 420 (2006).
- [71] L. Meyer, A. Eckart, R. Schödel, W. J. Duschl, K. Mužić, M. Dovčiak, and V. Karas, *Astron. Ap.* **460**, 15 (2006).

- [72] S. S. Doeleman, J. Weintroub, A. E. E. Rogers, R. Plambeck, R. Freund, R. P. J. Tilanus, P. Friberg, L. M. Zzurys, J. M. Moran, B. Corey, et al., *Nature (London)* **455**, 78 (2008).
- [73] V. L. Fish, American Astronomical Society, IAU Symposium #261. Relativity in Fundamental Astronomy: Dynamics, Reference Frames, and Data Analysis 27 April - 1 May 2009 Virginia Beach, VA, USA, #13.04; *Bulletin of the American Astronomical Society*, Vol. 41, p.889 **261**, 1304 (2009).
- [74] S. S. Doeleman, V. L. Fish, A. E. Broderick, A. Loeb, and A. E. E. Rogers, *Astrophys. J.* **695**, 59 (2009).
- [75] M. Mościbrodzka, C. F. Gammie, J. C. Dolence, H. Shiokawa, and P. K. Leung, *Astrophys. J.* **706**, 497 (2009).
- [76] A. E. Broderick, V. L. Fish, S. S. Doeleman, and A. Loeb, *Astrophys. J.* **697**, 45 (2009).
- [77] J. D. Schnittman and J. H. Krolik, *Astrophys. J.* **701**, 1175 (2009).
- [78] N. Metropolis, A. W. Rosenbluth, M. N. Rosenbluth, A. H. Teller, and E. Teller, *J. Chem. Phys.* **21**, 1087 (1953).
- [79] W. K. Hastings, *Biometrika* **57**, 97 (1970).
- [80] Throughout, changes per orbit are denoted by δ and changes over an arbitrary time interval by Δ .
- [81] Here and elsewhere, we ignore the distinction between the total orbital angular momentum, and the Newtonian angular momentum, which exhibits a slight additional “wobble” [40]. It is easy to show that the amplitude of the wobble is tiny given the parameters considered here.
- [82] A flat, $\gamma = 0$ distribution all the way out to ~ 1 pc is inconsistent with the observations. For the $\gamma = 0$ models, we are assuming (as in the other models) that the flat distribution is local to a volume $\ll 1$ pc, and normalizing the total mass to $(10, 30, 100)\mathcal{M}_{\odot}$ inside 1 mpc.